Fuel Regression Characteristics of Axial-Injection End-Burning Hybrid Rocket Using Nitrous Oxide

Ryota Okuda[1], Kodai Komizu[2],
Ayumu Tsuji[3], Takumi Miwa[4], Mai Fukada[5]
Graduate School of Engineering, Hokkaido University,
Sapporo, 060-8628, Japan

Shuichi Yokobori[6], Kentaro Soeda[7]
Institute for Photon Science and Technology, The University of Tokyo, Tokyo, 113-0033, Japan

and

Landon Kamps[8], Harunori Nagata[9]
Faculty of Engineering, Hokkaido University, Sapporo, 060-8628, Japan

This study is an investigation of fuel regression characteristics in an axial-injection end-burning hybrid rocket using nitrous oxide. Experiments were conducted using ϕ38 mm cylindrical fuel grains with an array of 0.8 mm ports made from curable. Previous studies of end-burning hybrid rockets used gaseous oxygen as the oxidizer. Nitrous oxide may be more suitable than the gaseous oxygen for use in space-based missions because of the weight savings associated with the oxidizer storage vessels, supply system, and motor mass. In this study, two types of nozzle closures were employed to increase the initial chamber pressure and promote

Presented as Paper 2020-3753 at AIAA Propulsion and Energy 2020 Forum, VIRTUAL EVENT, August 24-28, 2020

[1] Master's course student, Graduate School of Engineering, Hokkaido University, Sapporo, 060-8628, Japan.
[2] Master's course student, Graduate School of Engineering, Hokkaido University, Sapporo, 060-8628, Japan.
[3] Doctor's course student, Graduate School of Engineering, Hokkaido University, Sapporo, 060-8628, Japan.
[4] Master's course student, Graduate School of Engineering, Hokkaido University, Sapporo, 060-8628, Japan.
[5] Master's course student, Graduate School of Engineering, Hokkaido University, Sapporo, 060-8628, Japan.
[6] Specially-appointed researcher, Institute for Photon Science and Technology, The University of Tokyo, Tokyo, 113-0033, Japan.
[7] Specially-appointed researcher, Institute for Photon Science and Technology, The University of Tokyo, Tokyo, 113-0033, Japan.
[8] Specially Appointed Assistant Professor, Faculty of Engineering, Hokkaido University, Sapporo, 060-8628, Japan.
[9] Professor, Faculty of Engineering, Hokkaido University, Sapporo, 060-8628, Japan.

the formation of stabilized combustion in multiport fuels. The results of 12 firing tests showed that the regression rates when using nitrous oxide as the oxidizer were as high as that from previous research (0.61-4.5 mm/s at 0.25-0.75 MPa) using gaseous oxygen as the oxidizer. These high regression rates were nearly five times higher than that of experiments using single port fuels. It is clear from a visualization experiment that fuel flakes break off and travel downstream in solid form during firing, which could cause the fuel regression rate of multiport fuels to be higher than that of single port fuels.

Nomenclature

a = initial fuel area fraction as defined by Eq. (2)

A_f = fuel area

A_t = nozzle throat area

c^* = theoretical characteristic exhaust velocity

c^*_{ave} = average characteristic exhaust velocity

C_v = flow coefficient of the orifice

d = port diameter

d_{ex} = estimated port diameter

D = fuel diameter

D_t = nozzle throat area

L = fuel length

m = oxidizer port velocity exponent

$\dot{m}_f$ = fuel mass flow rate

$\dot{m}_{f,Curableresin}$ = fuel mass flow rate of curable resin

$\dot{m}_{f,PMMA}$ = fuel mass flow rate of curable resin

$\dot{m}_o$ = oxidizer mass flow rate

M_f = experimental fuel mass consumption during firing

$M_{f,cal}$ = calcurated fuel mass consumption during firing

n = pressure exponent

N = number of ports

O/F = oxidizer to fuel ratio

P_c = chamber pressure

P_{mo} = Pressure measured upstream of the orifice

ΔP = total pressure loss

ΔP_{in} = inlet pressure loss

ΔP_{out} = outlet pressure loss

ΔP_{pipe} = pressure loss for pipe flow

ΔP_{dev} = pressure loss coefficient

R = specific gas constant

Re = Reynolds number

r = correlation coefficient

T = temperature

t_f = firing duration

V_o = oxidizer port velocity

V_f = fuel regression rate

α = constant value

β = constant value

ζ_{in} = inlet pressure loss coefficient

ζ_{out} = outlet pressure loss coefficient

η = efficiency of characteristics exhaust velocity

λ = friction coefficient of pipe

μ = viscosity coefficient

ξ = coefficient of pressure loss in the approach section

ρ_f = fuel density (= 1191 kg/m^3 =)

ρ_o = oxidizer density

I. Introduction

Hybrid rockets have several advantages over solid and liquid rockets, such as safety, environmental friendliness, and low cost, because the fuel and oxidizer are stored in separate phases and typically do not contain toxic additives [1]. Conventional hybrid rockets (see Fig. 1), however, have several weaknesses, one of the most crucial being *O/F* (oxidizer-to-fuel mass ratio) shift during firing and throttling [2]. Although throttling capability is a virtue of hybrid rockets, the *O/F* shift that accompanies throttling leads to a loss of specific impulse. Even without any throttling, the *O/F* shift may occur because the burning surface area changes with time during firing.

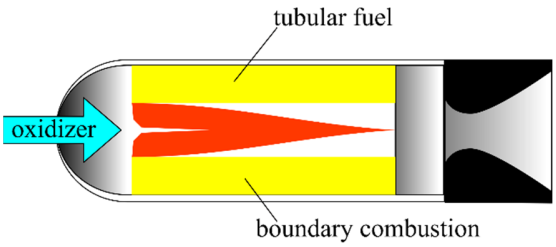

Fig. 1 Conventional hybrid rockets

To overcome these defects, Nagata et al. proposed an axial-injection end-burning hybrid rocket (EBHR) [3-6]. Figure 2a shows the concept sketch of this rocket. The motor uses a cylindrical fuel with an array of many small ports running in the axial direction, through which an oxidizer gas flows. The combustion proceeds with a diffusion flame stabilized at each port exit. Neighboring ports eventually merge because each port exit expands with time, as shown in Fig. 2b. When the end-burning mode is achieved, no *O/F* shift occurs during firing because the burning surface area no longer changes.

It is necessary to arrange numerous micro ports evenly across the fuel surface and satisfy more than approximately 95% effective density/volumetric loading to realize an EBHR [6,7]. Although this requirement is very strict and almost impossible to achieve by machining, it also means that EBHR enables to achieve very high volumetric filling rates (95%) compared to conventional types (typically less than 0.5) [7]. Nagata et al. used a high accuracy 3D printer to satisfy this requirement and succeeded in verifying EBHR combustion [7]. Nagata et al. successfully fired an additively manufactured grain with an. Since the advent of the 3D printer, research related to EBHR motors has progressed rapidly. Saito et al. investigated the regression characteristics under chamber pressures ranging from 0.1 MPa to 1.05 MPa using oxygen [8, 9]. They reported that the fuel regression characteristics shown as Fig. 3, in which

the pressure exponent was close to that reported by Hashimoto (= 0.951) [6]. The fuel regression rate equation shown in Fig. 3 is expressed as Eq. (1):

$$V_f = \alpha P_c^{\,n} \tag{1}$$

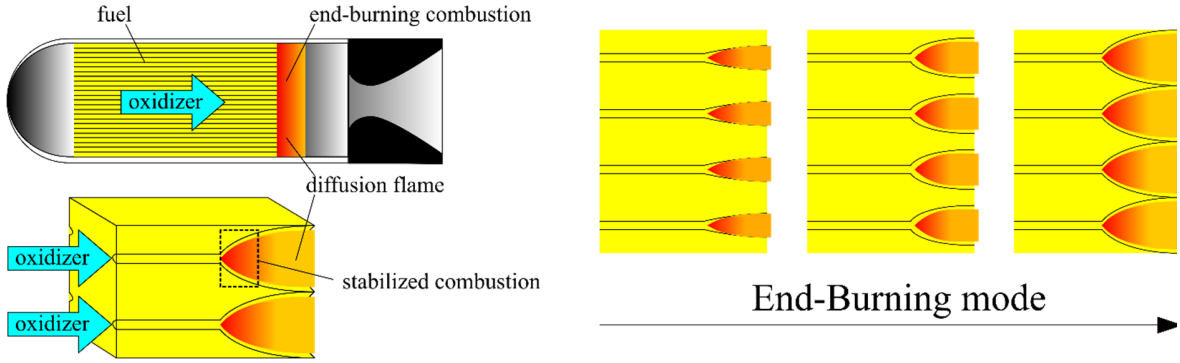

a) Stabilized combustion at the end face of the fuel b) Fuel regression during the initial transient

Fig. 2. Concept of an axial injection end-burning hybrid rocket

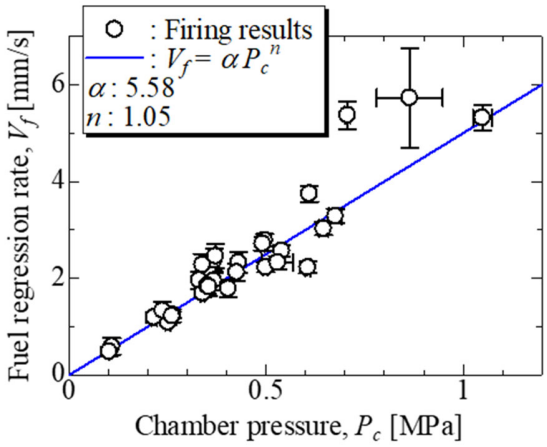

Fig. 3. The relationship between V_f and P_c with trend line [9]

The gaseous oxygen used as the oxidizer in these previous studies has the disadvantage that the weight of the structure increases when mounted on a spacecraft because it must be stored at very high pressures (>60 MPa) to approach the density of liquid oxygen at cryogenic temperatures. Furthermore, if liquid oxygen is on board, special equipment is required to return the liquid oxygen to the gas phase before injection, which adds weight and complexity to the system. Nitrous oxide has the following advantages for space applications [10]: (i) it is storable as a liquid at room temperature, (ii) it can self-pressurize, (iii) it will vaporize due to a pressure drop or temperature increase. One disadvantage of using N_2O in place of gaseous O_2 is a decrease in specific impulse upwards of 20s (roughly 6%). However, Kamps et al. reported that at a system level, N_2O is probably more suitable than O_2 for use in space-based

missions because of the weight savings associated with the oxidizer storage vessels, supply system, and motor mass, even though the specific impulse is lower [11].

Initial studies EBHR experiments (using oxygen) were conducted on a single port fuel grain, and based on those results, studies with multiport fuel grains followed. Omura et al. subsequently conducted research using N_2O as the oxidizer in a similar way, beginning with experiments using single port fuels under varying chamber pressures (0.1 MPa ~ 1.75MPa). They revealed that the pressure exponent is slightly above unity (= 1.19), but the fuel regression rate was roughly 1/5 of that when using oxygen [12]. When Omura et al. conducted experiments using multiport fuels based on the results of the single port experiments, the chamber pressures observed were far from the target values. They explained this discrepancy as resulting from the fact that stabilized combustion did not appear at each port exit, because the initial chamber pressure was too low. Therefore, they employed gaseous oxygen to increase the initial chamber pressure and succeeded in obtaining the end-burning mode. However, considering the added cost and complexity of a secondary oxygen flow related to system development and future (space) mission integration, it would be of great value to achieve stabilized combustion using only nitrous oxide.

Thus, the purpose of this study is to establish the experiment set-up for stabilized combustion of multiport fuels using only nitrous oxide and to investigate fuel regression characteristics in the end-burning mode.

II. Fuel Material

Figure 4 shows a fuel grain manufactured by a high accuracy 3D printer. It is an ultraviolet curable resin consisting of 80% to 90% acrylic acid ester, 5% hexamethylene acrylate, and a photopolymerization initiator. Table 1 shows the details of the fuel shape used in this study. The following equation gives the initial fuel filling rate:

$$a = \frac{\pi D^2/4 - N\pi d^2/4}{\pi D^2/4} = 1 - N\left(\frac{d}{D}\right)^2 \tag{2}$$

Equation (2) determines the initial fuel area fraction to obtain the optimal *O/F*.

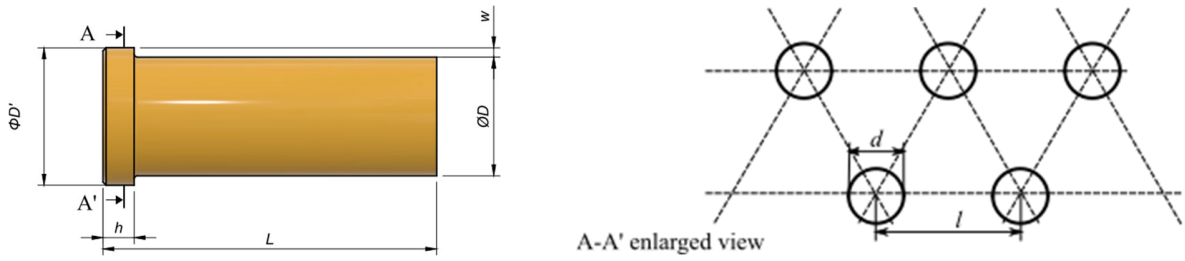

Fig. 4. Fuel shape

Table 1. Details of the fuel shape

Fuel outer diameter	D	[mm]	38	38
Port diameter	d	[mm]	0.8	0.8
Number of ports	N	[-]	337	253
Port interval	l	[mm]	2.3	2.2
Fuel axial length	L	[mm]	107	107
Flange diameter	D'	[mm]	44	44
Flange protrusion length	w	[mm]	3	3
Flange thickness	h	[mm]	10	10

Table 2 shows the basic properties of the fuel. Figure 5 shows the relationship between theoretical characteristic exhaust velocity c^* and oxidizer to fuel ratio O/F obtained by NASA-CEA [21] based on the properties as listed in Table 2.

Table 2. Properties of the fuel (curable resin)

Fuel density [kg/m^3]	ρ_f	1191
Standard enthalpy change of formation [kJ/mol]		-296.9636
CHO ratio [mol/mol]		16.0873 : 20.6143 : 3.96810

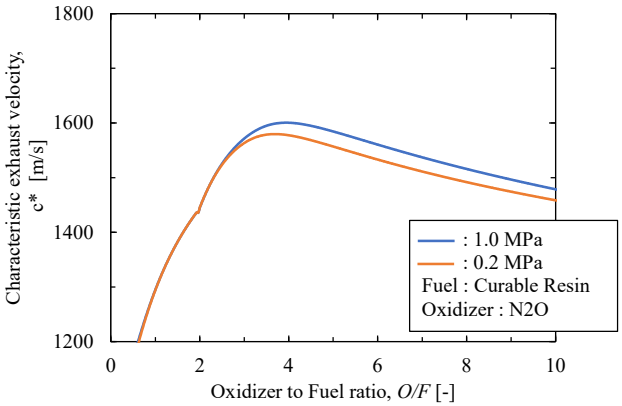

Fig. 5 c^* as a function of O/F and P_c

III. Experimental Apparatus

Figure 6 shows a schematic view of the experimental apparatus. It consists of a nitrous oxide tank, a nitrogen tank, two oxidizer lines with ball valves and needle valves for further adjusting the gas flow rate, one purge line and a combustion chamber. One of the needle valves in the parallel flow path is used for the micro flow line and the other is used for the main line. The oxidizer flow rate is adjusted by the opening degree of each needle valve. LabVIEW7 controlled the oxidizer flow timing and the operation of the valves. The oxidizer mass flow rate $\dot{m}_o$ [g/s] is calcurated from the pressure measured upstream of the orifice P_{mo} [MPa] as follows;

$$\dot{m}_o = C_v P_{mo} \tag{3}$$

where C_v is an experimentally determined coefficient of the orifice. This study used two types of orifices to obtain the desired $\dot{m}_o$. Flow rate tests conducted before firing tests gave the values of the coefficient as 5.43 g/s · MPa and 3.51 g/s · MPa.

A digital video camera monitored the exit of the combustion chamber. An orifice plate choked the oxidizer flow. During a firing test, KYOWA pressure transducers measured pressures at upstream and downstream of the orifice, and the combustion chamber. Details of the experimental equipment have been summarized in Table 3.

Figure 7 shows a schematic view of the test motor to visualize combustion. Unlike the combustion chamber shown in Fig. 6, the PMMA window was installed on the side of the combustion chamber for visualization. Moreover, the PMMA window was fixed and sealed from the outside with two O-rings. The contact surface between the PMMA window and the fuel has the same curvature as the fuel side surface. Furthermore, a highly transparent silicone sealant was applied between the window and the fuel to achieve a seal while maintaining visibility. Nitrous oxide flows into the combustion chamber from the left and enters the fuel grain. The nozzles had inner diameters of 4.0 mm, 5.4 mm, 6.2 mm, all of which had expansion ratios of unity. The test motor contains a water-cooling system, which consists of copper tubing and high heat conduction cement, to protect the combustion chamber against overheating and rupture during long-duration firing tests. Table 3 summarizes the details of the experimental equipment.

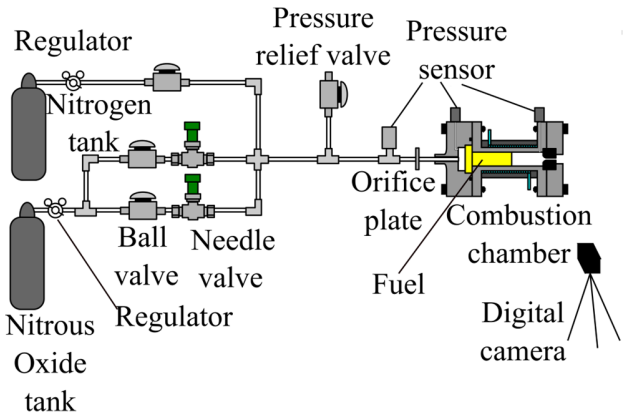

Fig. 6. Experimental apparatus

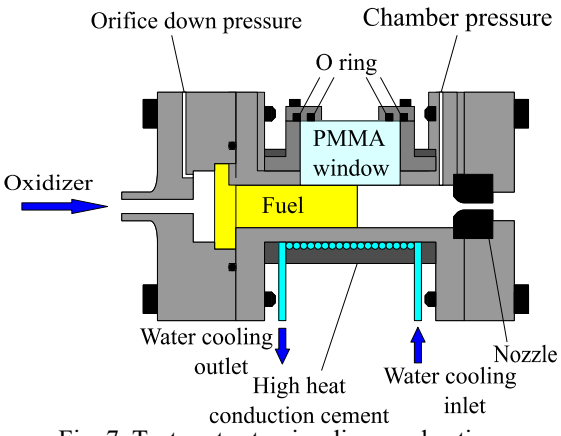

Fig. 7. Test motor to visualize combustion

Table 3. Details of experimental equipment

Item	Manufacture	Detail	Bias
Pressure sensor	Kyowa	PHB-A-10MP	0.0223 MPa
		PHB-A-5MP	0.0113 MPa
		PHB-A-2MP	0.0042 MPa
		PHB-A-2MP	0.0041 MPa
Electric scale	AND	Fz-300i	0.001g
Caliper	MonotaRO	Digital caliper	0.01 mm
Thermocouple	RS PRO	Type K	2.5 K
		Type T	0.5 K

Here, figures 8 and 9 show two experimental devices for conducting static firing tests without using oxygen for ignition. Previous studies suggested that stabilized combustion becomes possible by increasing the initial combustion chamber pressure [12]. To raise the initial combustion chamber pressure, we made two types of temporary nozzle restrictions. One is a nozzle closure, which plugs the nozzle and deflects from the nozzle when the chamber pressure exceeds a specific value. An O-ring was used for the nozzle closure to prevent it from quickly being ejected at low chamber pressures. However, the experiments confirmed that the nozzle closure did not always build up pressure with the same timing or blow off at the same pressure, so the repeatability of this method was not excellent. For this reason, Komizu et al. employed another type of closure: a melting nozzle to reduce the nozzle throat diameter so that the timing of pressurization does not affect the closure effectiveness [13]. A melting nozzle upstream of the original nozzle narrows the initial nozzle throat diameter to increase the initial combustion chamber pressure. The melting nozzle disappears with high reproducibility of the initial pressurization duration

Figure 10 explains the test sequence for ignition and oxidizer supply. At first, the nichrome wire, sponge, and nozzle closure (or the melting nozzle) are set. An AC power source heats the nichrome wire while feeding nitrous oxide into the chamber at a low rate (2.2×10^{-1} g/s). The sponge in front of the fuel grain end face ignites the entire end surface at once. The nitrous oxide supply was increased to the operating level when a flame was detected coming to the nozzle.

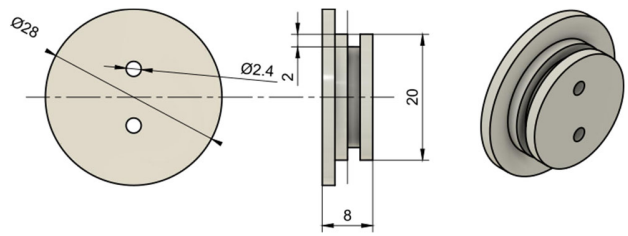

Fig. 8. Nozzle closure

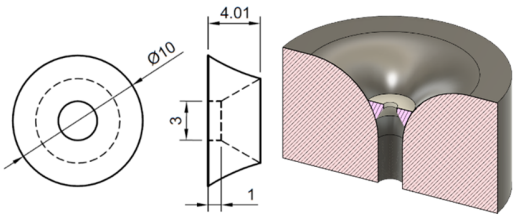

Fig. 9. Melting nozzle [13]

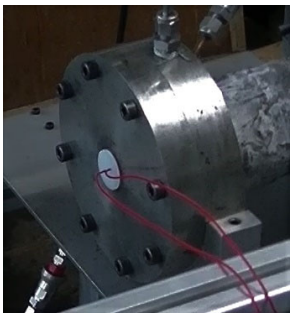

Setting nichrome wire and nozzle

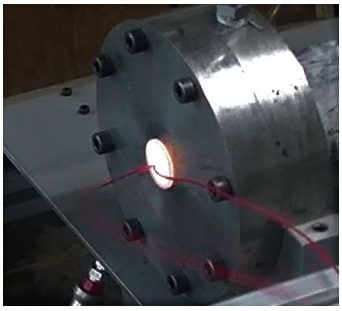

Flame detection

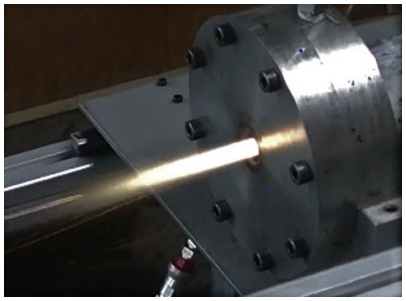

Oxidizer supply

Fig. 10. Test sequence for ignition and oxidizer supply

IV. Data reduction

A. An estimate of fuel area fraction

Hashimoto revealed that the oxidizer port velocity V_o [m/s] might influence the fuel regression rate by studying the combustion characteristics of a single port fuel [6]. Equation (4) expresses the oxidizer port velocity V_o based on the principle of mass conservation:

$$V_o = \frac{\dot{m}_o R T}{P_c A_f (1\text{-}a)} \tag{4}$$

The oxidizer port velocity changes if the initial fuel area fraction changes according to Eq. (4). Moreover, the initial fuel area fraction of the fuel may be different from the design value due to manufacturing error. Therefore, an experiment to estimate initial fuel area fraction was conducted by supplying oxidizer to the combustion chamber and measuring the pressure loss of the fuel upstream and downstream before each firing test. Substituting the measured pressure loss for Eq. (5), and the initial fuel area fraction was estimated according to Eq. (2).

$$\begin{aligned} \Delta P &= \Delta P_{in} + \Delta P_{out} + \Delta P_{pipe} + \Delta P_{dev} \\ \Delta P &= \zeta_{in} \frac{\rho_o}{2} V_o^2 + \zeta_{out} \frac{\rho_o}{2} V_o^2 + \lambda \frac{L}{d} \frac{\rho_o}{2} V_o^2 + \xi \frac{\rho_o}{2} V_o^2 \end{aligned} \tag{5}$$

where, ΔP, ΔP_{in}, ΔP_{out}, ΔP_{pipe}, ΔP_{dev}, ρ_o, λ, ζ_{in}, ζ_{out} and ξ express total pressure loss, inlet pressure loss, outlet pressure loss, pressure loss for pipe flow, the pressure loss in an approach section, oxidizer density, the friction coefficient of the pipe, inlet pressure loss coefficient, outlet pressure loss coefficient and coefficient of pressure loss in the approach section, respectively. An experiment estimating initial fuel area fraction was adjusted to obtain laminar

flow to avoid surface roughness effect. By assuming Hagen-Poiseuille flow, the friction coefficient of the pipe in the case of laminar flow is expressed as:

$$\lambda = \frac{64}{\mathrm{Re}} = \frac{64\,\mu}{\rho_o\, V_o\, d} \tag{6}$$

where μ expresses the viscosity coefficient [Pa・s]. The total pressure loss is as follows by substituting Eq. (5) for Eq. (6) and rearranging:

$$\Delta P = \frac{(\zeta_{in} + \zeta_{out} + \xi)\rho_o V_o^{\,2}}{2} + \frac{32\,\mu\, L\, V_o}{d^2} \tag{7}$$

The values of ζ_{in}, ζ_{out} and ξ used in this analysis were given by Ref. [14-19].

B. Fuel regression rate analysis

The fuel regression rate is expressed as:

$$V_f = \frac{\dot{m}_f}{\rho_f\, A_f\, a} \tag{8}$$

where $V_f, \dot{m}_f, \rho_o, A_f$ and a express fuel regression rate, fuel mass flow rate, fuel density, fuel area, initial fuel area fraction.

It is challenging to observe the fuel regression rate directly because the fuel is inside the combustion chamber. Therefore, this analysis employed a data reduction method, called a reconstruction technique, to obtain the fuel regression rate [20]. The reconstruction technique calculates the *O/F* history by solving the following equation:

$$\eta\, c^*\,(O/F,\, P_c) = \frac{P_c\, A_t}{\dot{m}_o \left(1 + \frac{1}{O/F}\right)} \tag{8}$$

where the theoretical characteristic exhaust velocity c^* was calculated using NASA-CEA [21]. The c^* efficiency η was adjusted so that the calculated total fuel mass consumption agrees with the experimentally measured value. Note that even if some of the fuel goes out through the nozzle without burning (as we will see later), the result will be reflected as a lower c^*efficiency so that the result gives an appropriate fuel flow rate. The reconstruction technique uses chamber pressure, oxidizer mass flow rate, and total fuel consumption as input data to estimate the characteristic exhaust velocity.

Using this method, we encountered the problem of multiple solutions reported by Nagata et. al. [20] when *O/F* is in the range from 1.9 to 2.01. Figure 11 plots the *O/F* history of Test2 in which the multiple solution problem was

observed. Thus, we employed the technique referred to as RT-5 (refer to Ref. [20]), which was proposed as a way to avoid the problem of multiple solutions with minimal loss to overall accuracy.

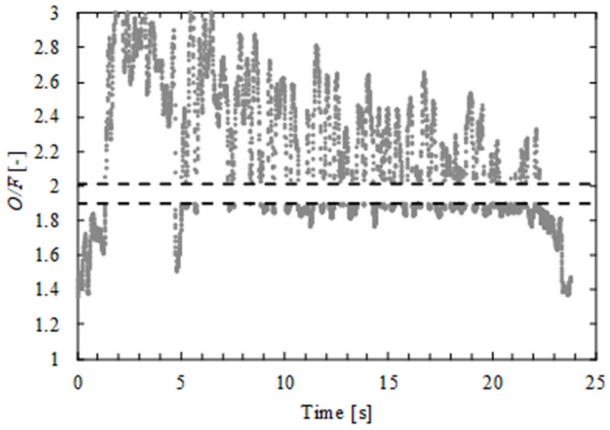

Fig. 11 Problem of multiple solutions (Test2)

First, the time-averaged characteristic exhaust velocity c^*_{ave} is calculated according to Eq. (9):

$$c^*_{ave} = \frac{\int_0^{t_f} P_c A_t dt}{\int_0^{t_f} \dot{m}_o dt + M_f} \tag{9}$$

Assuming that the characteristic exhaust velocity history can be approximated by its average, c^*_{ave}, we can calculate *O/F'* according to Eq. (10):

$$O/F' = \frac{\dot{m}_o c^*_{ave}}{P_c A_t - \dot{m}_o c^*_{ave}} \tag{10}$$

Inputing *O/F*' into the CEA code, and assuming that η and *O/F* relate to each other through Eq. (8), we solve the equation for *O/F*. This method allows us to avoid the convergent calculation from Eq. (2), meaning that Eq. (11) can overcome the difficulty of obtaining *O/F* when we encounter the multiple-solutions problem:

$$O/F = \frac{\dot{m}_o \eta c^*_{th}(P_c,\ O/F)}{P_c A_t - \dot{m}_o \eta c^*_{th}(P_c,\ O/F)} \tag{11}$$

Figure 12 shows the calculation flowchart for RT5.

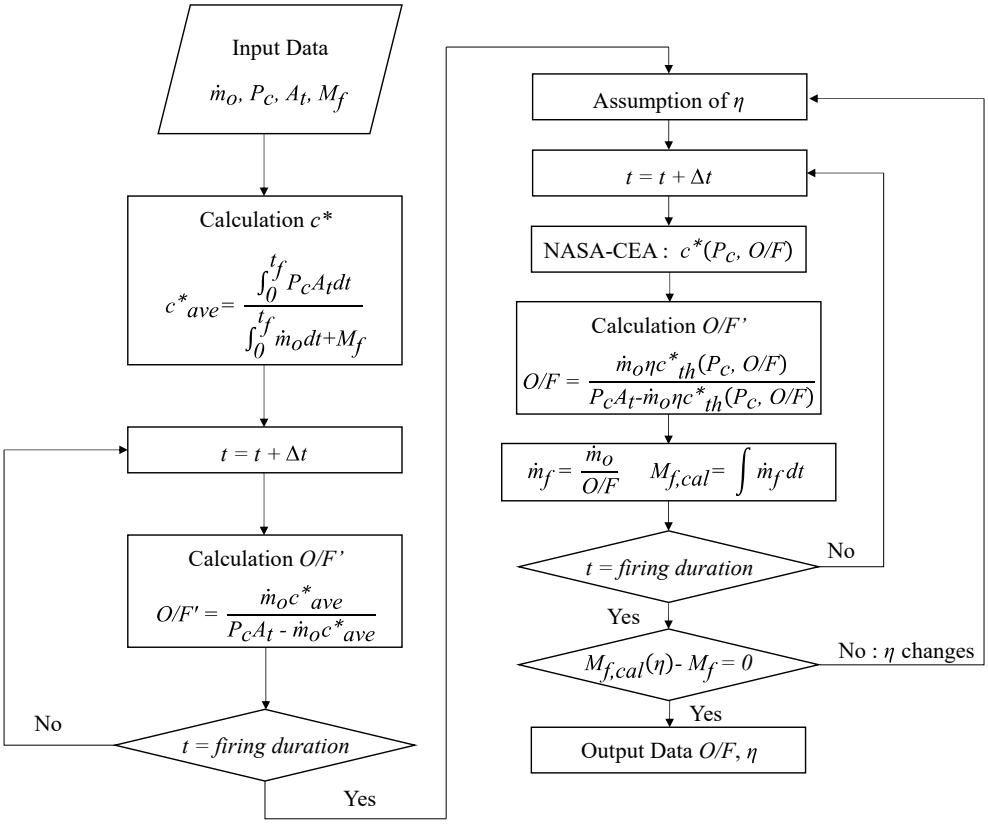

Fig. 12 Calculation flowchart for RT5

C. Error analysis

The data obtained by the experiments includes an error resulting from the bias and precision of the measurement devices. An error analysis evaluated the data accurately according to the law of error propagation [22]. The bias B_α for arbitrary test variable α is determined by Eq. (12):

$$B_\alpha{}^2 = \sum_i \left(\frac{\partial \alpha}{\partial x_i} B_{x_i} \right)^2 \tag{12}$$

where x_i is the parameter for α, B_{x_i} is the bias for x_i parameter error. $\partial\alpha/\partial x_i$ represent α sensitivity to x_i and is obtained by the gradient of α when x_i is increased by 10%. Equation (13) defines arbitrary test variables α was defined using x_i:

$$\alpha = \alpha\,(x_1, x_2, \ldots, x_n) \tag{13}$$

The following equations indicate dominant parameters for essential values in this study, including: the volumetric filling rate of the fuel a, the oxidizer mass flow rate $\dot{m}_o$, the fuel regression rate V_f, and the efficiency of characteristic exhaust velocity η.

$$\begin{gathered} a = a(\Delta P,\ \dot{m}_o,\ T,\ L_f) \\ \dot{m}_o = \dot{m}_o(C_v,\ P_{mo}) \\ V_f = V_f(P_c,\ \dot{m}_o,\ M_f,\ a) \\ \eta = \eta\left(P_c,\ \dot{m}_o,\ M_f\right) \end{gathered} \tag{14}$$

As an example, the *O/F* bias is obtained by expanding Eq. (15)

$$B_{O/F} = \sqrt{\left(\frac{\partial O/F}{\partial P_c}B_{P_c}\right)^2 + \left(\frac{\partial O/F}{\partial \dot{m}_o}B_{\dot{m}_o}\right)^2 + \left(\frac{\partial O/F}{\partial M_f}B_{M_f}\right)^2 + \left(\frac{\partial O/F}{\partial A_t}B_{A_t}\right)^2} \tag{15}$$

D. Effect of the PMMA window

During visualization experiment, not only the fuel but also the PMMA window gasifies. Miwa et al., who use a similar test apparatus, accounted for this effect analytically by the following method [23].

The sum of the fuel consumption and the PMMA consumption is used as input data of total fuel consumption for the reconstruction technique. The equilibrium calculation for c^* in the reconstruction technique is then carried out assuming that the fuel is 100% curable resin. This method is acceptable because the constituents of PMMA and the curable resin are almost the same, and the PMMA consumption was much less than the fuel consumption (around 5%). The fuel mass flow rate of the curable resin $\dot{m}_{f,Curableresin}$ was obtained by subtracting the PMMA mass flow rate $\dot{m}_{f,PMMA}$ from the calculated fuel mass flow rate $\dot{m}_f$ as follows.

$$\dot{m}_{f,CurableResin} = \dot{m}_f - \dot{m}_{f,PMMA} \tag{16}$$

The fuel regression rate V_f was calculated by the following equation under the assumptions that stabilized combustion appeared at all port exits to attain an end-burning mode, and the burning surface regressed uniformly.

$$V_f = \frac{\dot{m}_{f,CurableResin}}{\rho_f A_f a} \tag{17}$$

where A_f and ρ_f are the fuel area and the fuel density. We estimated the instantaneous PMMA mass flow rate from the shape and burning area of the PMMA window. Because the regression rate of PMMA window depends on the oxidizer mass flux G like a conventional hybrid rocket, $\dot{m}_{f,PMMA}$is determined only by the burning area under constant G. The burning area increases with the fuel regression, as shown in Fig. 13. By assuming the constant fuel

regression rate, it is estimated that the burning area and accordingly $\dot{m}_{f,PMMA}$ increases linearly over time, as Fig. 14 shows, where the x-axis and the y-axis are time and $\dot{m}_{f,PMMA}$, respectively. The gray area in Fig. 14 equals to the total PMMA consumption $\dot{m}_{f,PMMA}$. By measuring the ratio of the initial and the final burning area k from the shape of the window, instantaneous $\dot{m}_{f,PMMA}$ is obtained as follows.

$$\dot{m}_{f,PMMA}(t) = \frac{2(k-1)M_{f,PMMA}}{(1+k)t_f^2}t + \frac{2M_{f,PMMA}}{(1+k)t_f} \tag{18}$$

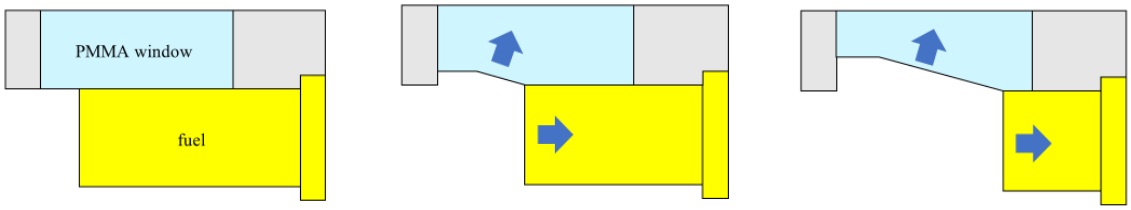

Fig. 13 Burning area changing [23]

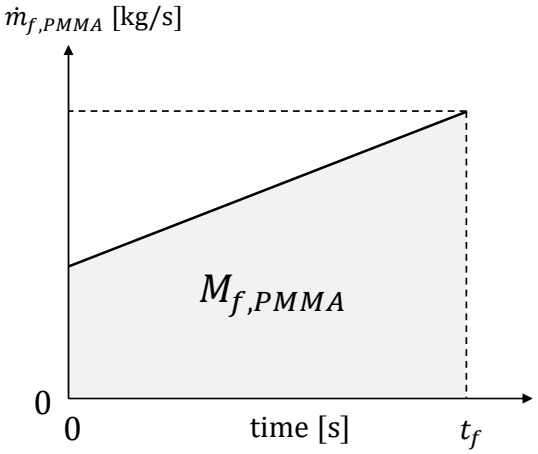

Fig. 14 $\dot{m}_{f,PMMA}$ history [23]

V. Results and Discussion

A. Firing test results

In total, 12 firing tests using nitrous oxide were conducted with varying oxidizer mass flow rates, nozzle throat diameters, and chamber pressure. A windowless combustion chamber was used for Tests 1 to 11. The visualization chamber was only used for Test 12. Table 4 summarizes all the test conditions: the initial fuel area fraction, its bias, the estimated mean port diameter, the number of ports, the nozzle throat diameter, flow coefficient of the orifice, method of building pressure.

Table 4. Test conditions using nitrous oxide

Test	a [-]	B_a [-]	d_{ex} [mm]	N [-]	D_t [mm]	C_v [g/s · MPa]	Method of building pressure [-]
1	0.841	0.159	0.826	337	6.2	5.43	NC
2	0.918	0.0190	0.685	253	4	5.43	NC
3	0.792	0.0521	0.943	337	6.2	5.43	NC
4	0.893	0.0263	0.677	337	5.4	5.43	NC
5	0.896	0.0252	0.667	337	5.4	5.43	MN
6	0.849	0.0953	0.806	337	5.4	5.43	MN
7	0.896	0.0255	0.669	337	5.4	5.43	MN
8	0.939	0.0160	0.510	337	5.4	5.43	MN
9	0.900	0.0374	0.754	253	5.4	3.51	-
10	0.890	0.0592	0.792	253	5.4	3.51	-
11	0.876	0.0648	0.842	253	5.4	3.51	-
12	0.900	0.0368	0.756	253	5.4	3.51	NC

NC : Nozzle Closure
MN : Melting Nozzle

Figures 15 and 16 show sample histories of chamber pressure and oxidizer mass flow rate, and sample histories chamber pressure and *O/F* of one of the test articles (Test-3), respectively. Figures 17 and 18 show sample histories of chamber pressure and oxidizer mass flow rate, and sample histories chamber pressure and *O/F* of one of the test articles (Test-8), respectively. Both *O/F* histories remain almost constant at steady state chamber pressure. Test-3 and Test-8 were the experiments using the nozzle closure and the melting nozzle, respectively. In the test using the nozzle closure, the chamber pressure gradually increases in time after the blow-off of the closure by pressurization, whereas, in the melting nozzle experiments, the pressure became steady immediately after melting.

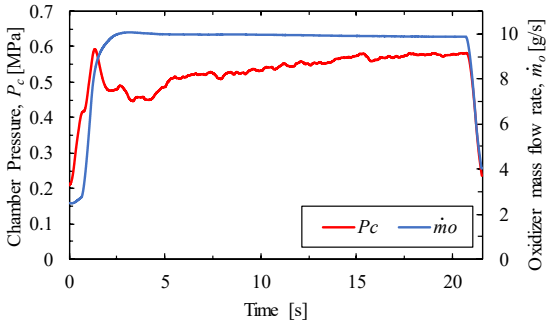

Fig. 15. Sample histories of chamber pressure and oxidizer mass flow rate (Test-3)

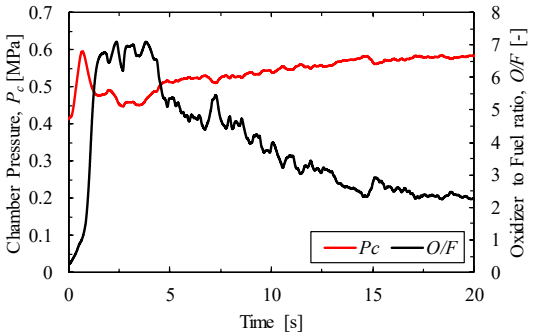

Fig. 16. Sample histories of chamber pressure and *O/F* (Test-3)

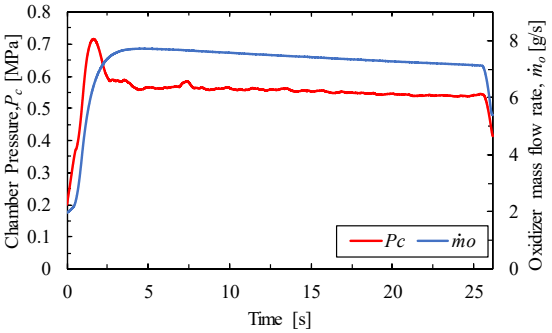

Fig. 17. Sample histories of chamber pressure and oxidizer mass flow rate (Test-8)

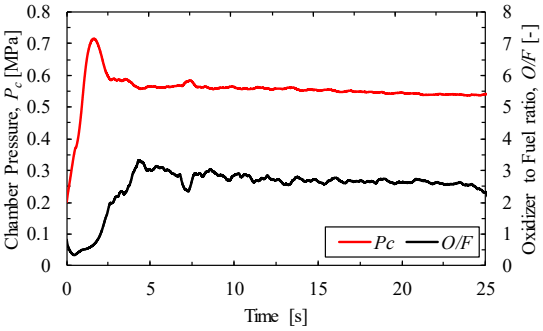

Fig. 18. Sample histories of chamber pressure and *O/F* (Test-8)

Table 5 summarizes the most pertinent data from these firing tests: nozzle throat diameter, firing duration, oxidizer mass flow rate, chamber pressure, fuel mass consumption, oxidizer port velocity, the efficiency of characteristic exhaust velocity, *O/F* (oxidizer-to-fuel-mass ratio), fuel regression rate, fuel regression rate calculated by using time average and each bias. A data reduction method called a reconstruction technique [15] was employed to estimate the efficiency of characteristic exhaust velocity, *O/F,* and fuel regression rate.

Table 5. Firing results using nitrous oxide

Test	t_f [s]	$\dot{m}_o{}^*$ [g/s]	$P_c{}^*$ [MPa]	M_f [g]	$V_o{}^*$ [m/s]	η [-]	O/F^* [-]	$V_f{}^*$ [mm/s]	$B_{\dot{m}_o}$ [g/s]	B_{V_o} [m/s]	B_η [-]	$B_{O/F}$ [-]	B_{V_f} [mm/s]
1**	30.7	7.41	0.41	86.0	5.15	0.764	1.98	3.36	0.732	0.964	0.0613	0.202	0.797
2**	48.6	3.81	0.43	89.6	4.87	0.659	1.88	1.67	0.339	0.446	0.0517	0.161	0.211
3**	19.4	9.85	0.58	64.7	3.72	0.810	2.04	4.51	0.885	0.388	0.0565	0.204	0.675
4**	13.1	9.71	0.74	73.6	5.56	0.819	2.22	3.63	0.875	0.523	0.0625	0.199	0.473
5***	38.7	3.71	0.24	32.5	6.74	0.804	4.98	0.612	0.541	1.10	0.0823	0.704	0.126
6***	38.3	4.81	0.34	63.2	4.25	0.770	2.76	1.53	0.590	0.663	0.0735	0.360	0.323
7***	18.0	6.34	0.44	27.9	6.26	0.823	4.29	1.22	0.670	0.682	0.0620	0.426	0.181
8***	23.5	7.31	0.55	83.1	10.0	0.802	2.08	2.77	0.726	1.20	0.0690	0.209	0.343
9	51.0	5.25	0.35	56.8	6.96	0.763	3.97	1.10	0.431	0.633	0.0458	0.364	0.143
10	36.7	7.71	0.59	93.2	5.43	0.798	1.97	2.70	0.613	0.545	0.0494	0.190	0.414
11	43.6	7.68	0.59	90.4	4.82	0.820	2.36	3.32	0.619	0.500	0.0469	0.265	0.483
12#	45.1	3.85	0.43	67.9	4.03	1.14	1.59	1.95	0.304	0.387	0.0706	0.112	0.226

*Average value during the steady-state region of firing test

**Firing test with the nozzle closure

***Firing test with the melting nozzle

#Firing test with the visualization chamber

B. Fuel regression characteristics

Figure 19 shows the relationship between the fuel regression rate and chamber pressure for all tests, as listed in Table 4. The empirical constants of the regression rate formula, Eq. (1), were determined by the least-squares method to be n = 1.30 and $\alpha = 6.20$, with a correlation coefficient of 0.786. The correlation coefficient shows the correlation between the curve in Fig. 19 and the fuel regression rate obtained in the experiments. The pressure exponent is far from unity in this result, although mostly all experiments on EBHR until now observe pressure exponents near unity. Moreover, this result did not match the expectations based on the results of the previous research using single-port fuels that the fuel regression rates were roughly five times lower than in experiments using oxygen as the oxidizer. When comparing Fig. 3 with Fig. 20, the fuel regression rates using oxygen and nitrous oxide showed similar values. Also, Hitt et al. report that the fuel regression rates in their experiments using nitrous oxide ranged from approximately 0.21 mm/s at 0.207 MPa to 1.44 mm/s at 1.054 MPa [24], although the fuel type was different from the present experiment. Therefore, the results of these experiments do not match the findings of by Hitt et al. either.

In previous studies, Saito et al. reported that the fuel regression rate had a positive correlation with the chamber pressure and a negative correlation with the oxidizer port velocity [8]. The variations of V_o shown in Table 5 are significant, implying that the oxidizer port velocity would have some effect on the fuel regression rate. Here, the fuel

regression rate equation will be modified to include oxidizer port velocity to quantify the effect of this parameter. This modified equation is expressed as Eq. (13):

$$V_f = \beta P_c^{\,n} V_o^{\,m} \tag{13}$$

where, V_f, β, P_c, V_o express fuel regression rate [mm/s], a constant value [mm/s/(MPa)^n/(m/s)^m], chamber pressure [MPa], and oxidizer port velocity [m/s], respectively. The empirical constants of the regression rate formula, Eq. (13), were determined by the least-squares method to be n; 1.32, β; 17.1 and m; - 0.605 with a correlation coefficient of 0.838 in Fig. 20 and a correlation coefficient of 0.443 in Fig. 21. We can see in Fig. 21 that the oxidizer port velocity has a negative correlation with the fuel regression rate, although there is a significant variation.

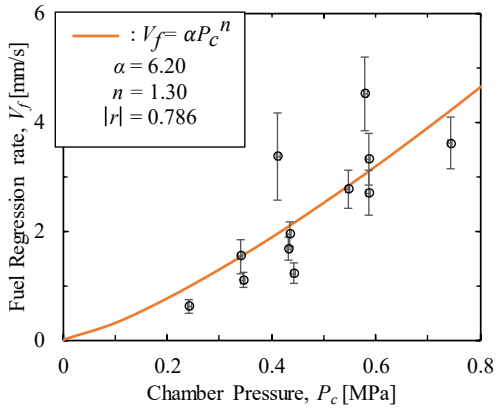

Fig. 19 The relationship between V_f and P_c in the case of nitrous oxide

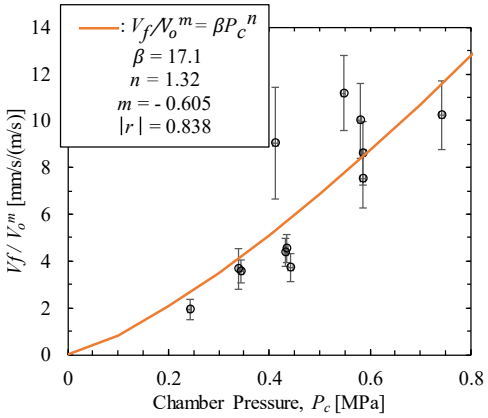

Fig. 20. The relationship between $V_f/V_o^{\,m}$ vs. chamber pressure in the case of nitrous oxide

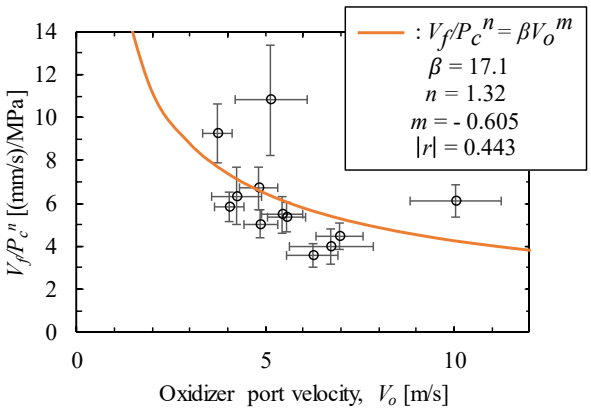

Fig. 21. The relationship between $V_f/P_c^{\,n}$ vs. oxidizer port velocity in the case of nitrous oxide

C. Visualization verification

As mentioned above, the fuel regression rate obtained in this study did not match that of the previous research using the single port fuels. One possible explanation for the finding is that, unlike the previous study, the fuel did not regress in stabilized combustion mode. Thus, a visualization experiment was conducted to directly observe the conditions during firing. Figures 22 and 23 are a series of time marching pictures of the combustion chamber captured through the PMMA window in Test 12 of this study and a test using gaseous oxygen from a previous study. The red ellipses indicate the location of the diffusion flame region. As these figures show, the diffusion flame forms at the fuel end surface and propagates in the upstream direction. Although it is hard to ascertain from the images alone, it is clear from the videos of Test 12 that large (~2 mm) fuel flakes break off near the end surface of the fuel and flow downstream within the combustion gas. Figures 24 and 25 are enlarged pictures from each test. The white ellipses in Fig. 25 shows the bell-shaped fuel regression fuel shape at the port exits typical of stabilized combustion. On the contrary, in Fig. 24, the test in which nitrous oxide was the oxidizer, it could be seen that cracks propagated upstream faster than the diffusion flame. Thus, either the bell-shape fuel regression expected of stabilized combustion was not formed, or was obscured by the surrounding fuel cracks. This result indicates that the propagation speed of cracks and flaking contributed to the fuel regression rate in the nitrous oxide cases.

Figure 26 is the pictures of the side of the fuel after the visualization experiment. The parts surrounded by the white line indicate the crack on the side of the fuel. As these figure show, it can also be confirmed from the fuel after firing that the fuel cracks occurred during the experiment.

Here, we compare the fuels after the visualization experiments with the other fuels after the firing tests. Figures 27 through 31 show some of the other fuels after experimentation. These figures do not show any significant cracks as shown in Fig.26. Figure 32 shows the fuel after the firing test using oxygen [25]. Since the combustion regress without changing the burning surface area in this case using O2, the fuel after firing has a clean flat burning surface area. However, after the experiment using nitrous oxide, the fuel had a skewed burning surface area. This may be due to the fact that the fuel burns with irregular cracks, and the burning surface area is not constant. In addition, as shown by the white ellipses in each figure, the sides of the fuel cracked irregularly, and there were also traces of partial sharpness. For these reasons, the fuel may be regressing with irregular cracking in the experiment using nitrous oxide.

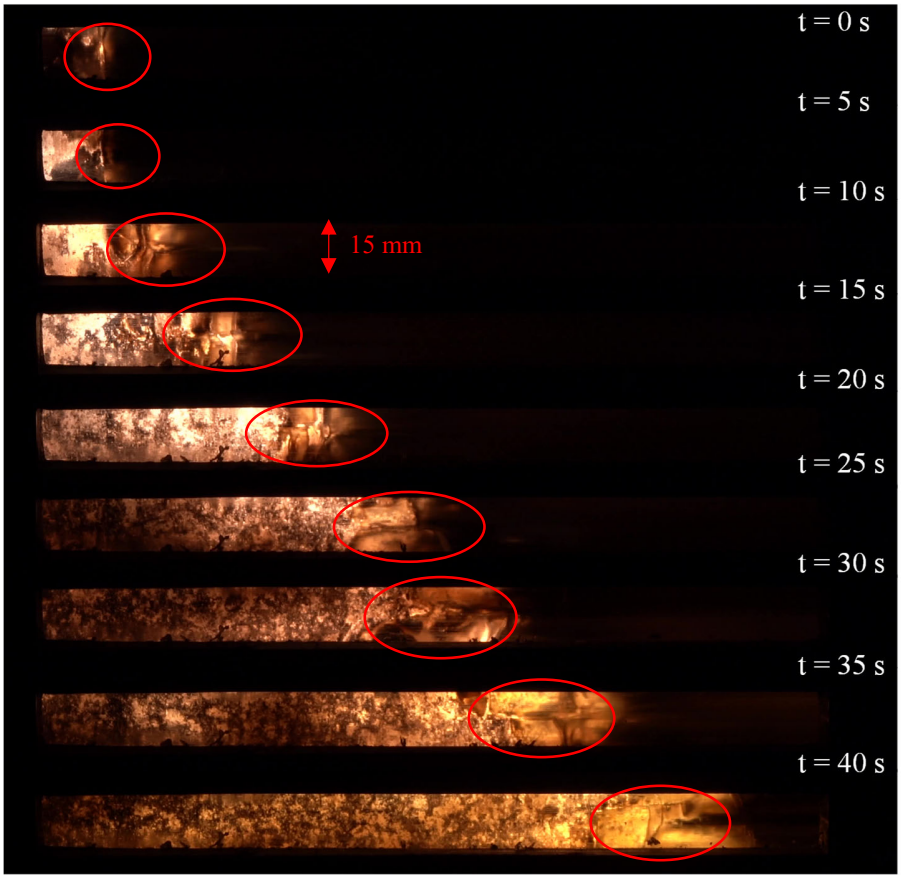

Fig. 22. Flame spread in Test 12

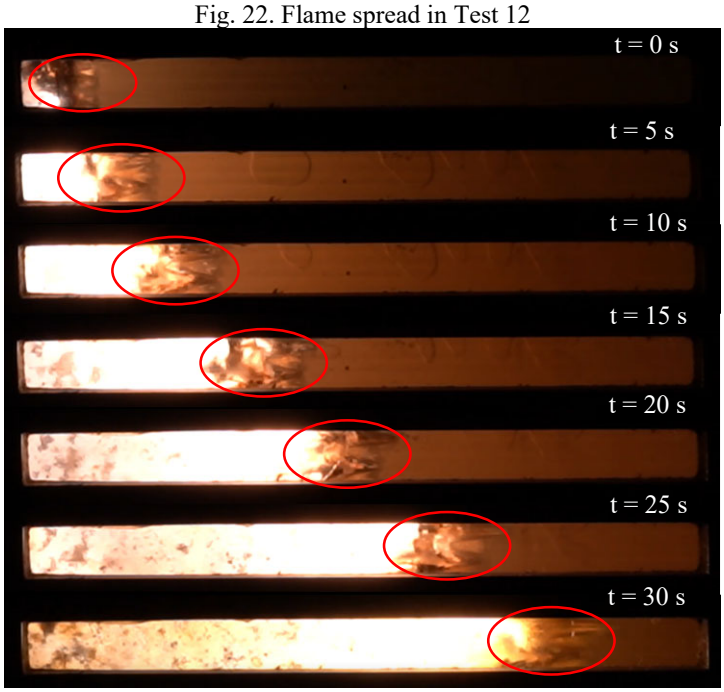

Fig.23. Flame spread in the test using O2[23]

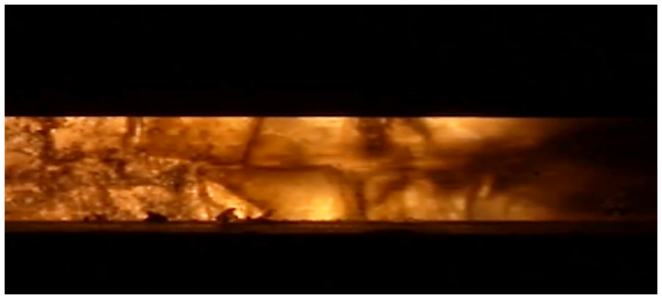

Fig. 24. Visualization of combustion of nitrous oxide

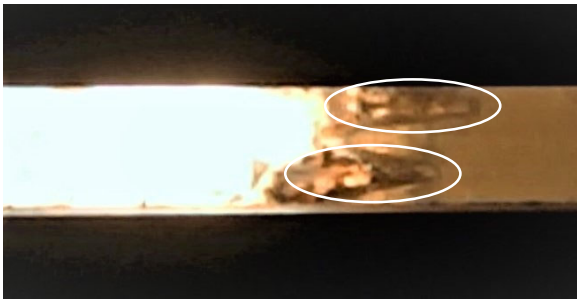

Fig. 25. Visualization of combustion of oxygen

Fig. 26. The side of the fuel after the visualization experiment (Test 12)

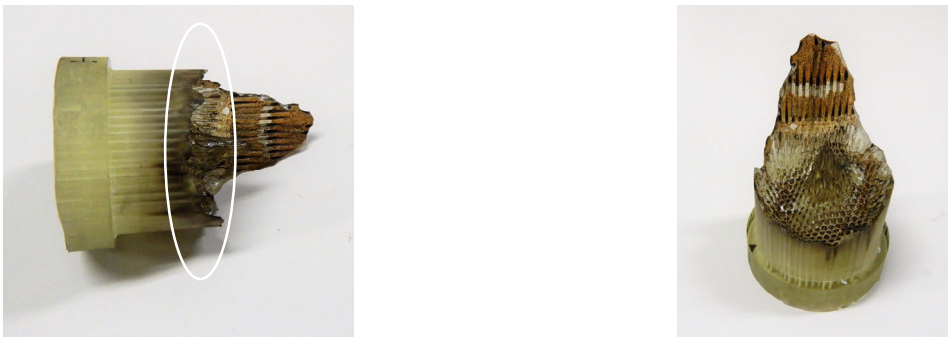

Fig. 27. The side of the fuel after the visualization experiment (Test 1)

Fig. 28. The side of the fuel after the visualization experiment (Test 2)

Fig. 29. The side of the fuel after the visualization experiment (Test 4)

Fig. 30. The side of the fuel after the visualization experiment (Test 10)

Fig. 31. The side of the fuel after the visualization experiment (Test 11)

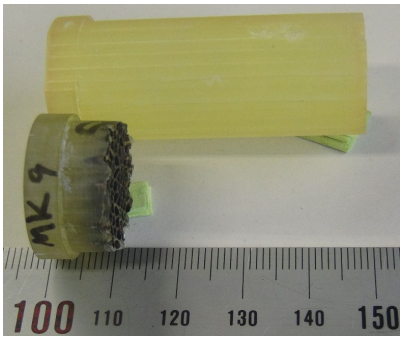

Fig.32 Fuel grain before (upper) and after (lower) firing using O2 [25]

Figures 33 and 34 are the schematics of the fuel regression in the case of oxygen and nitrous oxide (present study), respectively, which explain the difference between them. In the fuel regression with oxygen, the decomposition velocity of fuel determines the fuel regression rate, although small particles also break off or "splatter" from the end tip between neighboring ports. In the fuel regression with nitrous oxide, the crack propagation speed determines the fuel regression rate, and large fuel flakes are ejected. According to this hypothesis, the fuel regression rate of the multiport fuel becomes faster than that of single port fuel. Moreover, the cause for the scatter in the fuel regression rate in Fig. 20 may be that the amount of fuel flakes ejected differs in each experiment. Figure 35 shows the relationship between the efficiency of characteristic exhaust velocity and *O/F* for oxygen and nitrous oxide cases, respectively. The efficiency of characteristics exhaust velocity for nitrous oxide is lower than that when using oxygen. This result shows that fuel flakes may have exited the nozzle unburned, causing the observed decreases in efficiency.

Okutani et al. observed that when unburned particles pass through the nozzle unburned, conspicuously large pressure spikes occur in the chamber pressure history [26]. The cause of these pressure spikes was nozzle clogging by unburned particle ejections. However, as Figs. 15 and 17 show, the chamber pressure histories do not show any large pressure spikes, despite the visual confirmation that fuel flakes form and break off near the diffusion flame zone. Thus, it seems possible that the fuel flakes add to the overall (gas) fuel mass flow rate, but are mostly consumed by hot combustion gas before exiting the nozzle. In other words, this is not the stabilized combustion, but a new fuel regression mode. The new fuel regression mode, which shows no large pressure spikes and high fuel regression rates, is attractive for propulsion system applications, and needs to be further investigated. Only a 15 mm span of the 38 mm

diameter fuel could be observed through the combustor window, thus it was not possible to verify how the entire fuel end-surface burns. Additional visualization experiments are necessary to check for the new fuel regression mode.

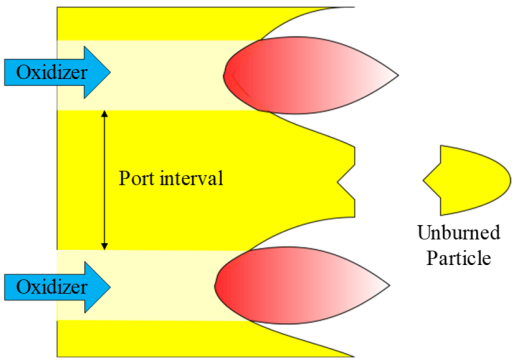

Fig. 33. Fuel splatter observed in previous research with O_2

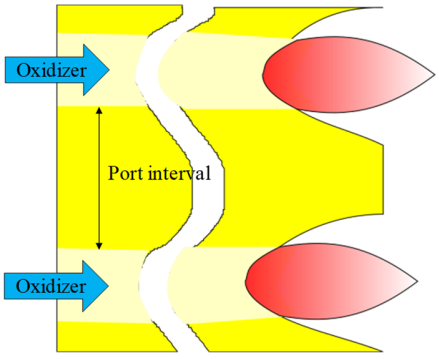

Fig. 34. The fuel flaking observed in this study

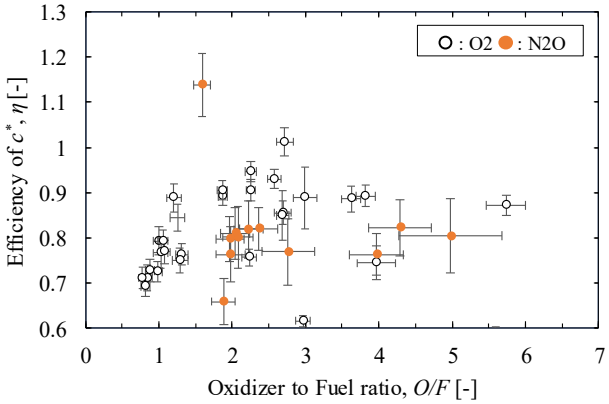

Fig. 35. The relationship between η and O/F

VI. Conclusion

In this study, the authors investigated the fuel regression characteristics of end-burning hybrid rockets using nitrous oxide. Previous research using nitrous oxide on a multiport fuel showed that stabilized combustion was not possible. In this study, a nozzle closure or a melting nozzle was employed to increase the initial chamber pressure and promote the formation of stabilized combustion in multiport fuels. The results of 12 firing tests showed that the regression rates when using nitrous oxide as the oxidizer were as high as that from previous research (0.61-4.5 mm/s at 0.25-0.75 MPa) using gaseous oxygen as the oxidizer, which did not match expectations based on the previous research experiments using nitrous oxide as the oxidizer with single-port fuels. Furthermore, the pressure exponent was larger than unity (n = 1.30), which is larger than is expected for end-burning hybrid rockets. A possible explanation for these

results is that the primary combustion mode was not stabilized combustion, but another, yet unreported, combustion mode. To check the combustion mode during firing, a visualization experiment was conducted in which the fuel regression rate could be observed directly. The results showed that the end-burning mode was not the only contribution to fuel mass consumption, but some portion of fuel flakes break off and are consumed before exiting the nozzle. This end-burning mode may be a new combustion mode. However, only part of the combustion was visualized, and it was not possible to confirm how the entire fuel burns in this way. Since this new combustion mode results in high fuel regression rates and stable chamber pressure, it is attractive for propulsion applications. Thus, future work needs to visualize the entire combustion to check the new combustion mode.

Acknowledgments

This research was supported by the Japanese Ministry of Education, Culture, Sports, Science and Technology as: Grant-in-Aid for Scientific Research (C) 17K06943 and 19K04832. This work was partially supported by JST COI Grant Number JPMJCE1313.

References

[1] Chiaverini, M. j., Kuo, K. K., "Fundamentals of Hybrid Rocket Combustion and Propulsion," *Progress in Astronautics and Aeronautics*, AIAA, Reston, VA, 2007, pp. 37-125.

[2] Karabeyoglu, A., Toson, E., and Evans, B., "O/F Shift in Hybrid Rockets," *50th AIAA/SAE/ASEE Joint Propulsion Conference*, AIAA Paper 2014-3851, July 2014.
doi: https://doi.org/10.2514/6.2014-3851

[3] Nagata, H., Okada, K., Sanda, T., Kato, T., Akiba, R., Satori, S., and Kudo, I., "Combustion Characteristics of Fibrous Fuels for Dry Towel Hybrid Rocket Motor," *Journal of Space Technology and Science*, Vol. 13, No. 1, 1997, pp. 11–16.
doi: https://doi.org/10.11230/jsts.13.1_11

[4] Kato, T., Hashimoto, N., Nagata, H., Akiba, R., and Kudo, I., "A Preliminary Study of End-Burning Hybrid Rocket, Part 1: Combustion Stability", *Journal of the Japan Society for Aeronautical and Space Sciences*, Vol. 49, No. 565, 2001, pp. 33–39.
doi: https://doi.org/10.2322/jjsass.49.33

[5] Hashimoto, N., Kato, T., Nagata, H., Akiba, R., and Kudo, I., "A Preliminary Study of End-Burning Hybrid Rocket, Part 2: Combustion Characteristics", *Journal of the Japan Society for Aeronautical and Space Sciences*, Vol. 49, No. 565, 2001, pp. 40–47.

doi: https://doi.org/10.2322/jjsass.49.40

[6] Hashimoto, N., "End-Burning Type Hybrid Rocket," Ph.D. Dissertation, Hokkaido University, Sapporo, Japan, 2004.

[7] Nagata, H., Teraki, H., Saito, Y., Kanai, R., Yasukochi, H., Wakita, M., and Totani, T., "Verification Firings of End-Burning Type Hybrid Rockets," *Journal of Propulsion and Power*, Vol. 33, No. 6, 2017, pp.1473–1477.
doi: https://doi.org/10.2514/1.B36359

[8] Saito, Y., Yokoi, T., Yasukochi, H., Soeda, K., Totani, T., Wakita, M., and Nagata, H., "Fuel Regression Characteristics of a Novel Axial-Injection End-Burning Hybrid Rocket," *Journal of Propulsion and Power*, Vol. 34, No. 1, 2018, pp. 247-259.
doi: https://doi.org/10.2514/1.B36369

[9] Saito, Y., Kimino, M., Tsuji, A., Okutani, Y., Soeda, K., and Nagata, H., "High Pressure Fuel Regression Characteristics of Axial-Injection End-Burning Hybrid Rockets" *Journal of Propulsion and Power*, Vol. 35, No. 2, 2019.
doi: https://doi.org/10.2514/1.B37135

[10] National Institute of Standards and Technology, NIST Chemistry WebBook, http://webbook.nist.gov/cgi/cbook.cgi?ID=C10024972&Mask=10 (accessed on 1 February 2020).

[11] Kamps, L., Molas-Roca, P., Uchiyama, E., Takanashi, T., Nagata, H., "Development of N2O/HDPE Hybrid Rocket for Microsatellite Propulsion", *70 th International Astronautical Congress*, Paper code IAC-19,C4,8-B4.5A,12,x49906, 2019

[12] Omura, K., "Combustion Characteristics of Nitrous Oxide Axial-injection End-burning Hybrid Rocket," MS thesis, Hokkaido University, Sapporo, Japan, 2017.

[13] Komizu, K., "Combustion Characteristics of Axial-Injection End-Burning Hybrid Rocket under Throttling Operation Using N2O", MS thesis, Hokkaido University, Sapporo, Japan, 2019.

[14] Weisbach, J., *Mechanics of engineering and of machinery*, 2nded, J. Willey & Sons, New York, 1896, pp.1003.

[15] Richter, H., *Rohrhydraulik : ein Handbuch zur praktischen Strömungsberechnung*, Springer-Verlag Berlin Heidelberg, Berlin, 1958, pp. 172.
doi: https://doi.org/ 10.1007/978-3-642-52164-5

[16] Gibson, A.H., *Hydraulics and Its Applications*, 5thed, Constable & Company, London, 1952, pp. 91.

[17] Tokio, U., "Loss of Head of Water Flow due to Sudden Eccentric Enlargement of Area of a Pipe," *Journal of the Japan Society of Mechanical Engineer*s, Vol. 2, No. 7, 1936, pp. 254–256
doi: https://doi.org/10.1299/kikai1935.2.254

[18] Bender, E., "Druckverlust bei laminarer Strömung im Rohreinlauf," *Chemie Ingenieur Technik*, Vol. 41, No. 11, 1969, pp. 682.
doi: https://doi.org/10.1002/cite.330411108

[19] McComas, S.T., "Hydrodynamic Entrance Length for Ducts of Arbitray Cross Section," *Journal of Basic Engineering*,

Vol. 89, No. 4, 1967, pp.847.
doi: https://doi.org/10.1115/1.3609713

[20] Nagata, H., Nakayama, H., Watanabe, M., Wakita, M., Totani, T., "Accuracy and applicable range of a reconstruction technique for hybrid rockets," *Advances in Aircraft and Spacecraft Science*, vol. 1, No. 3, 2014, pp. 273-289.
doi: https://doi.org/10.12989/aas.2014.1.3.273

[21] S. Gordon and B. J. McBride, "Computer Program for Calculation of. Complex Chemical Equilibrium Compositions and Aplications," NASA Reference Publication", RP-1311, 1994.

[22] Frederick, R. A., and Greiner, B. E., "Laboratory-Scale Hybrid Rocket Motor Uncertainty Analysis," *Journal of Propulsion and Power*, Vol. 12, No. 3, 1996, pp. 605–611.
doi: https://doi.org/10.2514/3.24076

[23] Miwa, T., Tsuji, A., Okuda, R., Yokobori, S., Soeda,K., Kamps, L., and Nagata, H., "Visualization of Fuel Regression Rate in Axial-Injection End-Burning Hybrid Rocket," *AIAA Propulsion and Energy 2020 Forum*, AIAA Paper 2020-3766, 2020.
doi: https://doi.org/10.2514/6.2020-3766

[24] Hitt, M. A. and Frederick, R. A., Jr., "Experimental Evaluation of a Nitrous-Oxide Axial-Injection, End-Burning Hybrid Rocket," Journal of Propulsion and Power, Vol. 33, No. 6 (2017), pp. 1555-1560, November-December 2017. doi:https://doi.org/10.2514/1.B36439

[25] Saito, Y., Yokoi, T., Yasukochi., H., Soeda, K., Totani, T., Wakita, M., and Nagata, H., "Fuel Regression Characteristics of a Novel Axial-Injection End-Burning Hybrid Rockets" Journal of Propulsion and Power, Vol. 34, No. 1, 2018.
doi: https://doi.org/10.2514/1.B36369

[26] Okutani, Y., "Investigation of Combustion Characteristics under High Pressure in Axial Injection End Burning Hybrid Rockets," MS thesis, Hokkaido University, Sapporo, Japan, 2018.